Electronic Supplementary Material (ESI) for Journal of Materials Chemistry A.
This journal is © The Royal Society of Chemistry 2023

Supplementary Information

Exploring the Mobility of Cu in Bimetallic Nanocrystals to Promote Atomic-Scale Transformations under a Reactive Gas Environment

Jette K. Mathiesen, Sofie Colding-Fagerholt, Kim D. Jensen, Jack K. Pedersen, Tom Vosch, Jan Rossmeisl, Stig Helveg and Kirsten M. Ø. Jensen**

Table of contents

A. Rietveld refinements of glass-supported monometallic nanocrystals

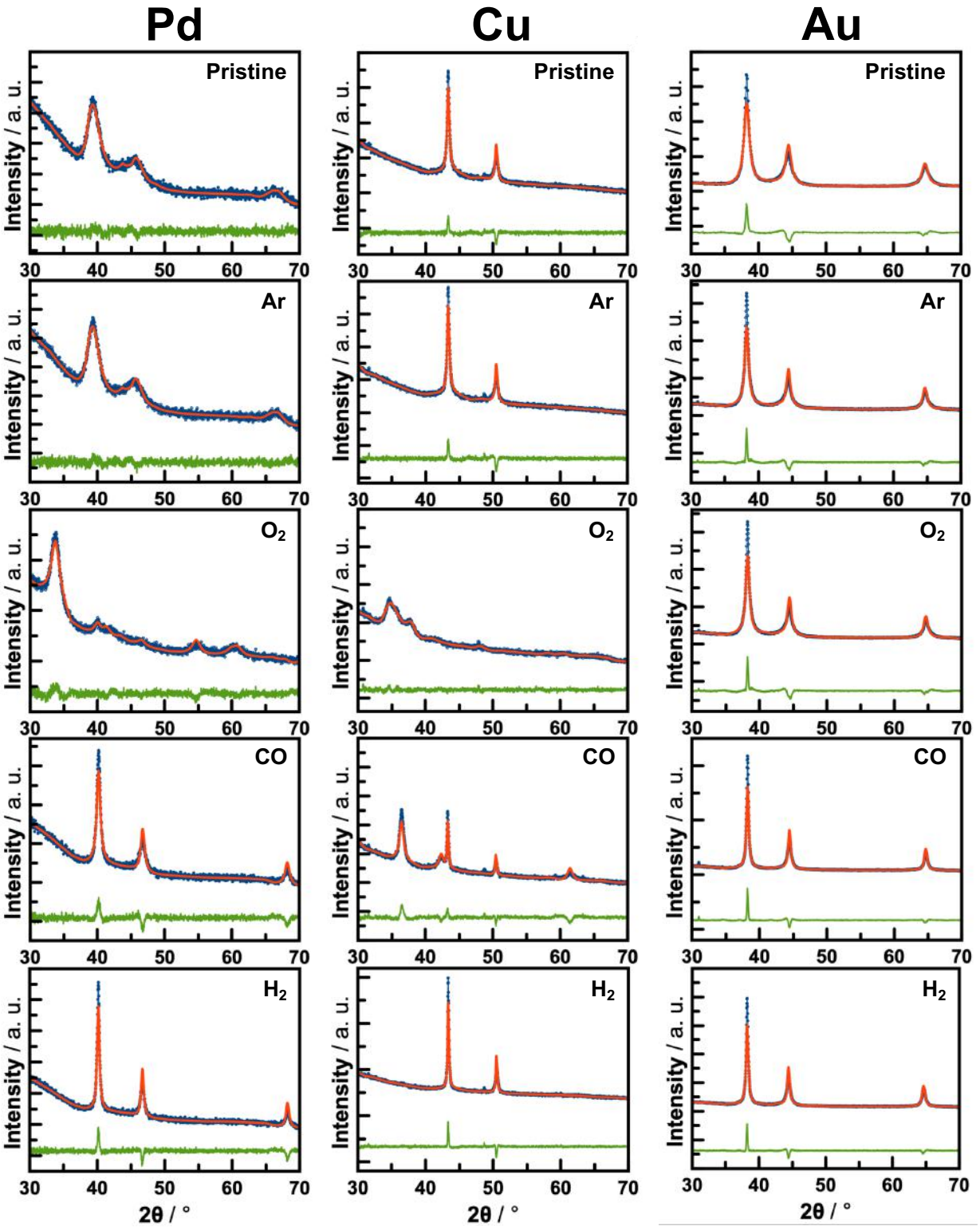

Fig. S1. Rietveld refinements of glass-supported monometallic nanocrystals resulting from different gas exposures at 300 °C.

Table S1. Refined values from Rietveld refinements of glass-supported Pd nanocrystals resulting from different gas exposures at 300 °C.

	Pristine	**Ar**	**O_2**	**CO**	**H_2**
R_{wp} / %	13.10	13.00	30.40	24.00	23.70
$Scale_{Pd}$	3.95×10^{-3} ($\pm0.13\times10^{-3}$)	3.79×10^{-3} ($\pm0.17\times10^{-3}$)	2.46×10^{-4} ($\pm0.27\times10^{-4}$)	1.51×10^{-3} ($\pm0.19\times10^{-4}$)	1.34×10^{-3} ($\pm0.13\times10^{-4}$)
a_{Pd} / Å	3.98 ($\pm0.22\times10^{-2}$)	3.98 ($\pm0.18\times10^{-2}$)	3.90 ($\pm0.16\times10^{-2}$)	3.89 ($\pm0.58\times10^{-3}$)	3.89 ($\pm0.36\times10^{-3}$)
Y_{Pd}	2.69 ($\pm0.41\times10^{-1}$)	2.53 ($\pm0.55\times10^{-1}$)	1.09 (±0.11)	0.59 ($\pm0.96\times10^{-2}$)	0.36 ($\pm0.53\times10^{-2}$)
Crystallite $size_{Pd}$ / nm	3.28	3.49	8.09	14.96	24.51
$Scale_{PdO}$	-	-	0.33 ($\pm0.66\times10^{-4}$)	-	-
a_{PdO} / Å	-	-	3.09 ($\pm0.91\times10^{-3}$)	-	-
c_{PdO} / Å	-	-	5.25 ($\pm0.25\times10^{-2}$)	-	-
Y_{PdO}	-	-	1.28 ($\pm0.42\times10^{-1}$)	-	-
Crystallite $size_{PdO}$ / nm	-	-	6.89	-	-
Phase composition (Pd/PdO) / %	-	-	13.50 (±1.50) / 86.50 (±2.66)	-	-

Table S2. Refined values from Rietveld refinements of glass-supported Cu nanocrystals resulting from different gas exposures at 300 °C.

	Pristine	**Ar**	**O_2**	**CO**	**H_2**
R_{wp} / %	21.70	23.70	11.30	30.40	23.30
$Scale_{Cu}$	$6.73\times\cdot10^{-3}$ ($\pm0.95\times10^{-4}$)	8.20×10^{-3} ($\pm0.11\times10^{-3}$)	-	2.85×10^{-3} ($\pm0.59\times10^{-4}$)	8.19×10^{-3} ($\pm0.13\times10^{-3}$)
a_{Cu} / Å	3.61 ($\pm0.41\times10^{-3}$)	3.61 ($\pm0.28\times10^{-3}$)	-	3.62 ($\pm0.37\times10^{-3}$)	3.61 ($\pm0.31\times10^{-3}$)
Y_{Cu}	0.32 ($\pm0.67\times10^{-2}$)	0.16 ($\pm0.45\times10^{-2}$)	-	0.16 ($\pm0.65\times10^{-2}$)	0.16 ($\pm0.49\times10^{-2}$)
Crystallite $size_{Cu}$ / *nm*	27.57	55.15	-	55.15	55.15
$Scale_{Cu2O}$	-	-	9.41×10^{-3} ($\pm0.68\times10^{-3}$)	4.51×10^{-3} ($\pm0.91\times10^{-4}$)	-
a_{Cu2O} / Å	-	-	4.43 ($\pm0.32\times10^{-2}$)	4.27 ($\pm0.49\times10^{-3}$)	-
Y_{Cu2O}	-	-	3.65 (±0.13)	0.69 ($\pm0.16\times10^{-1}$)	-
Crystallite $size_{Cu2O}$ / nm	-	-	2.42	12.79	-
Phase composition (Cu/Cu_2O) / %	-	-	-	25.45 (±0.66) **/** 74.55 (±1.92)	-
$Scale_{CuO}$	-	-	4.32×10^{-3} ($\pm0.47\times10^{-3}$)	-	-
a_{CuO} / Å	-	-	4.75 ($\pm0.36\times10^{-2}$)	-	-
b_{CuO} / Å	-	-	3.57 ($\pm0.35\times10^{-2}$)	-	-
c_{CuO} / Å	-	-	5.17 ($\pm0.37\times10^{-2}$)	-	-
Y_{CuO}	-	-	1.45 ($\pm0.89\times10^{-1}$)	-	-
Crystallite $size_{CuO}$ / nm	-	-	6.09	-	-
Phase composition (Cu_2O/CuO) / %	-	-	66.30 (±6.24) **/** 33.70 (±4.20)	-	-

Table S3. Refined values from Rietveld refinements of glass-supported Au nanocrystals resulting from different gas exposures at 300 °C.

	Pristine	**Ar**	**O_2**	**CO**	**H_2**
R_{wp} / %	16.10	18.50	18.60	18.60	17.20
$Scale_{Au}$	3.18×10^{-3} ($\pm0.45\times10^{-4}$)	2.02×10^{-3} ($\pm0.17\times10^{-4}$)	2.01×10^{-3} ($\pm0.18\times10^{-4}$)	1.76×10^{-3} ($\pm0.13\times10^{-4}$)	1.65×10^{-3} ($\pm0.11\times10^{-4}$)
a_{Au} / Å	4.08 ($\pm0.50\times10^{-3}$)	4.08 ($\pm0.25\cdot10^{-3}$)	4.08 ($\pm0.27\times10^{-3}$)	4.08 ($\pm0.18\times10^{-3}$)	4.08 ($\pm0.16\times10^{-3}$)
Y_{Au}	0.87 ($\pm0.15\times10^{-1}$)	0.59 ($\pm0.67\cdot10^{-2}$)	0.59 ($\pm0.73\times10^{-2}$)	0.34 ($\pm0.43\times10^{-2}$)	0.34 ($\pm0.37\times10^{-2}$)
Crystallite $size_{Au}$ / nm	10.14	14.96	14.96	25.95	25.95

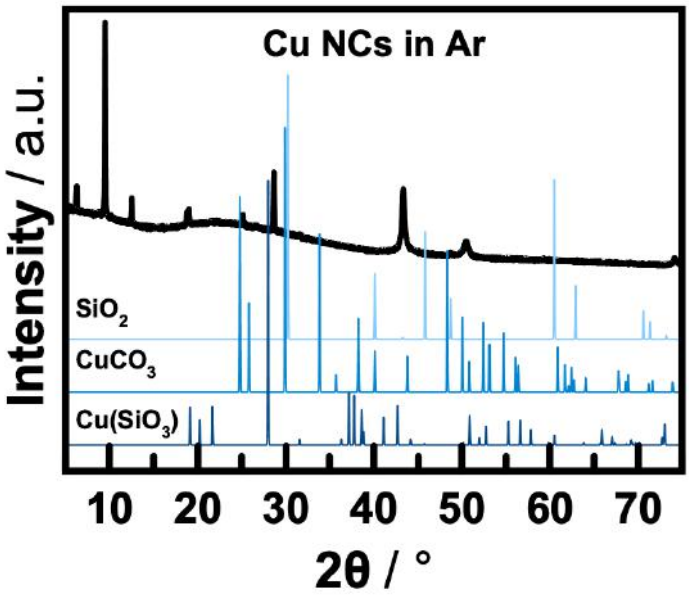

Fig. S2. Cu NCs treated in Ar, where the low angle scattering peaks have been compared to relevant structures from the database. However, due to the lack of description, the peaks are most likely to arise due to unreduced Cu^{2+} precursor.

B. Rietveld refinements of glass-supported bimetallic nanocrystals

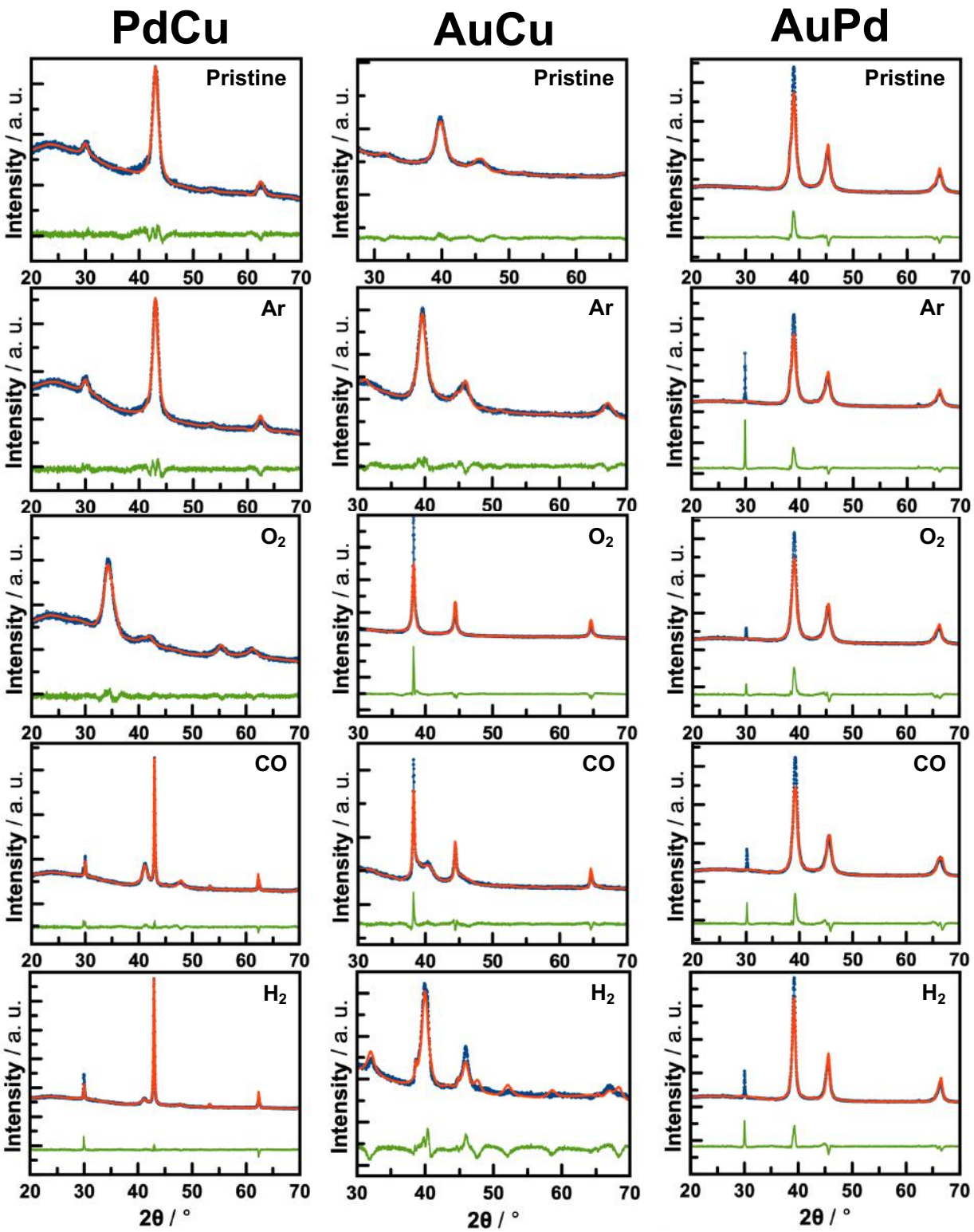

Fig. S3. Rietveld refinements of glass-supported bimetallic nanocrystals resulting from different gas exposures at 300 °C.

Table S4. Refined values from Rietveld refinements of glass-supported PdCu nanocrystals resulting from different gas exposures at 300 °C.

	Pristine	**Ar**	**O_2**	**CO**	**H_2**
R_{wp} / %	16.50	15.90	23.60	12.00	17.60
$Scale_{B2}$	2.84×10^{-2} ($\pm0.19\times10^{-3}$)	2.95×10^{-3} ($\pm0.18\cdot10^{-3}$)	-	1.49×10^{-2} ($\pm0.79\times10^{-4}$)	2.27×10^{-2} ($\pm0.11\times10^{-3}$)
a_{B2} / Å	2.97 ($\pm0.83\times10^{-3}$)	2.98 ($\pm0.72\times10^{-3}$)	-	2.98 ($\pm0.14\times10^{-3}$)	2.98 ($\pm0.12\times10^{-3}$)
Y_{B2}	1.13 ($\pm0.90\times10^{-2}$)	1.05 ($\pm0.79\times10^{-2}$)	-	0.13 ($\pm0.76\times10^{-3}$)	0.13 ($\pm0.67\times10^{-3}$)
$Crystallite\ size_{B2}$ / nm	7.81	8.40	-	67.87	67.87
$Scale_{Pd}$	-	-	1.56×10^{-4} ($\pm0.25\times10^{-4}$)	-	-
a_{Pd} / Å	-	-	3.84 ($\pm0.24\times10^{-2}$)	-	-
Y_{Pd}	-	-	1.03 (±0.18)	-	-
$Crystallite\ size_{Pd}$ / nm	-	-	8.57	-	-
$Scale_{PdO}$	-	-	6.72×10^{-3} ($\pm0.12\times10^{-3}$)	-	-
a_{PdO} / Å	-	-	3.04 ($\pm0.77\times10^{-3}$)	-	-
c_{PdO} / Å	-	-	5.21 ($\pm0.22\times10^{-2}$)	-	-
Y_{PdO}	-	-	1.43 ($\pm0.36\times10^{-1}$)	-	-
$Crystallite\ size_{PdO}$ / nm	-	-	6.17	-	-
$Scale_{A1}$	-	-	-	3.99×10^{-3} ($\pm0.54\times10^{-4}$)	1.71×10^{-3} ($\pm0.59\times10^{-4}$)
a_{A1} / Å	-	-	-	3.80 ($\pm0.26\times10^{-3}$)	3.80 ($\pm0.51\times10^{-3}$)
Y_{A1}	-	-	-	0.99 ($\pm0.16\times10^{-1}$)	0.96 ($\pm0.39\times10^{-1}$)
$Crystallite\ size_{A1}$ / nm	-	-	-	8.91	9.19
Phase composition (Pd/PdO) / %	-	-	4.54 (±0.73) / 95.46 ($\pm$ 2.46)	-	-
Phase composition (B2/A1) / %	-	-	-	47.38 (±0.43) / 52.62 (±0.81)	76.11 (±0.78) / 23.89 (±0.86)

Table S5. Refined values from Rietveld refinements of glass-supported AuCu nanocrystals resulting from different gas exposures at 300 °C.

	Pristine	**Ar**	**O_2**	**CO**	**H_2**
R_{wp} / %	12.30	17.00	30.60	18.10	25.00
$Scale_{AuCu}$	1.69×10^{-3} ($\pm0.86\times10^{-4}$)	9.05×10^{-4} ($\pm0.45\times10^{-4}$)	-	5.55×10^{-3} ($\pm0.91\times10^{-4}$)	4.33×10^{-3} ($\pm0.44\times10^{-4}$)
a_{AuCu}/ Å	4.023 ($\pm0.82\times10^{-3}$)	4.05 ($\pm0.86\times10^{-3}$)	-	3.96 ($\pm0.29\times10^{-2}$)	3.95 ($\pm0.59\cdot10^{-3}$)
c_{AuCu}/ Å	3.72 ($\pm0.13\times10^{-2}$)	3.75 ($\pm0.17\times10^{-2}$)	-	3.73 ($\pm0.33\times10^{-2}$)	3.82 ($\pm0.76\times10^{-3}$)
Y_{AuCu}	1.41 ($\pm0.52\times10^{-1}$)	1.14 ($\pm0.50\times10^{-1}$)	-	3.61 ($\pm0.88\times10^{-1}$)	1.13 ($\pm0.20\times10^{-1}$)
Crystallite $size_{AuCu}$ / nm	6.26	7.74	-	2.44	7.81
$Scale_{Au}$	1.55×10^{-2} ($\pm0.72\times10^{-4}$)	1.39×10^{-3} ($\pm0.30\times10^{-4}$)	1.17×10^{-3} ($\pm0.17\times10^{-4}$)	4.39×10^{-4} ($\pm0.44\times10^{-5}$)	4.82×10^{-5} ($\pm0.35\times10^{-5}$)
a_{Au} / Å	3.93 ($\pm0.37\times10^{-3}$)	3.94 ($\pm0.25\times10^{-3}$)	4.08 ($\pm0.28\times10^{-3}$)	4.08 ($\pm0.15\times10^{-3}$)	4.04 ($\pm0.55\times10^{-3}$)
Y_{Au}	1.94 ($\pm0.49\times10^{-1}$)	1.39 ($\pm0.21\times10^{-1}$)	0.32 ($\pm0.74\times10^{-2}$)	0.19 ($\pm0.38\times10^{-2}$)	0.24 ($\pm0.32\times10^{-1}$)
Crystallite $size_{Au}$ / nm	4.55	6.35	27.57	46.44	36.77
$Scale_{Au3Cu}$	-	-	-	3.53×10^{-4} ($\pm0.22\times10^{-4}$)	-
a_{Au3Cu} / Å	-	-	-	4.04 ($\pm0.66\times10^{-3}$)	-
Y_{Au3Cu}	-	-	-	0.88 ($\pm0.54\times10^{-1}$)	-
Crystallite $size_{Au3Cu}$ / nm	-	-	-	10.03	-
Phase composition (AuCu/Au) / %	58.15 (±3.35) / 41.85 (±2.57)	69.34 (±1.49) / 30.66 (±1.65)	-	-	97.92 (±1.38) / 2.08 (±0.15)
Phase composition (AuCu/Au/ Au_3Cu) / %	-	-	-	81.40 (±1.76) / 11.28 (±0.20) / 7.32 (±0.47)	-

Table S6. Refined values from Rietveld refinements of glass-supported AuPd nanocrystals resulting from different gas exposures at 300 °C.

	Pristine	**Ar**	**O_2**	**CO**	**H_2**
R_{wp} / %	16.40	18.20	19.40	20.60	15.40
$Scale_{AuPd}$	4.59×10^{-2} ($\pm0.67\times10^{-4}$)	3.95×10^{-3} ($\pm0.72\times10^{-4}$)	3.39×10^{-3} ($\pm0.12\times10^{-3}$)	2.44×10^{-3} ($\pm0.11\times10^{-3}$)	3.13×10^{-3} ($\pm0.75\times10^{-4}$)
a_{AuPd} / Å	3.99 ($\pm0.31\times10^{-3}$)	3.99 ($\pm0.34\times10^{-3}$)	3.99 ($\pm0.45\times10^{-3}$)	3.96 ($\pm0.51\times10^{-3}$)	3.98 ($\pm0.27\times10^{-3}$)
Y_{AuPd}	0.75 ($\pm0.99\times10^{-2}$)	0.73 ($\pm0.11\times10^{-1}$)	0.71 ($\pm0.15\times10^{-1}$)	0.62 ($\pm0.18\times10^{-1}$)	0.44 ($\pm0.79\times10^{-2}$)
Crystallite $size_{AuPd}$ / nm	11.77	12.09	12.43	14.23	20.05
$Scale_{Au}$	6.36×10^{-4} ($\pm0.42\times10^{-4}$)	6.17×10^{-4} ($\pm0.44\times10^{-4}$)	9.14×10^{-4} ($\pm0.76\times10^{-4}$)	1.52×10^{-3} ($\pm0.70\times10^{-4}$)	9.21×10^{-4} ($\pm0.48\times10^{-4}$)
a_{Au} / Å	4.05 ($\pm0.71\times10^{-3}$)	4.05 ($\pm0.76\times10^{-3}$)	4.03 ($\pm0.79\times10^{-3}$)	4.00 ($\pm0.51\times10^{-3}$)	4.00 ($\pm0.44\times10^{-3}$)
Y_{Au}	0.88 ($\pm0.44\times10^{-1}$)	0.85 ($\pm0.45\times10^{-1}$)	0.78 ($\pm0.35\times10^{-1}$)	0.68 ($\pm0.19\times10^{-1}$)	0.55 ($\pm0.18\times10^{-1}$)
Crystallite $size_{Au}$ / nm	10.03	10.38	11.31	12.98	16.04
Phase composition (AuPd/Au) / %	84.21 (±1.84) / 15.79 (±1.07)	82.61 (±2.20) / 17.39 (±1.29)	73.59 (±3.65) / 26.41 (±2.36)	54.54 (±3.11) /45.46 (±2.57)	71.91 (±2.38) / 28.09 (±1.59)

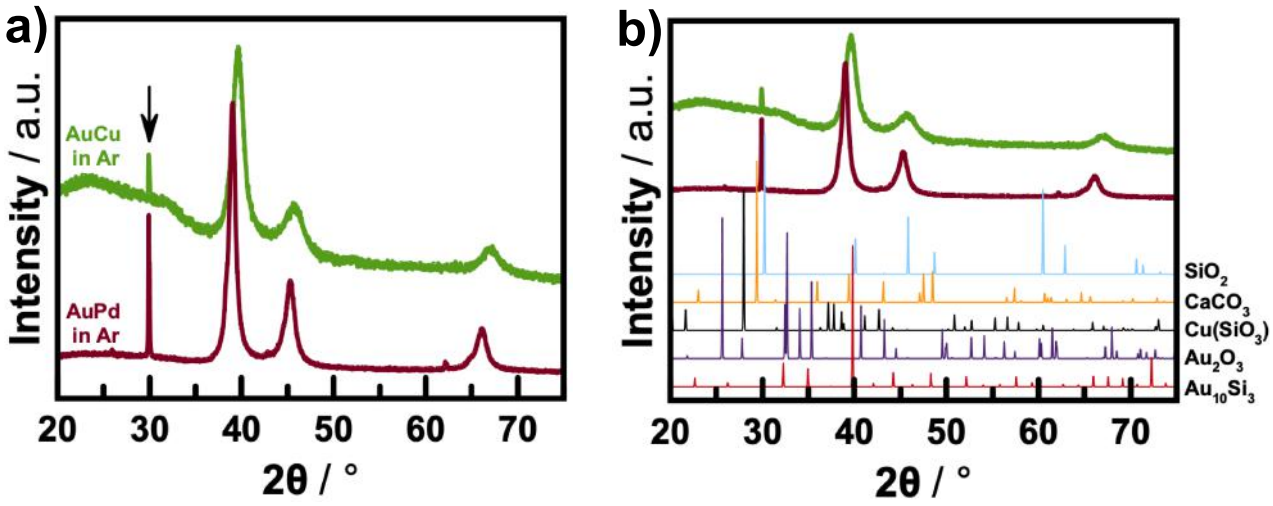

Fig. S4. (a) AuCu and AuPd NCs treated in Ar. (b) Comparing the peak at 30° 2θ (highlighted in (a) with an arrow) with relevant structures from the database. However, due to the lack of comparable structural features, the peaks are most likely to arise due to unreduced Au^{3+} precursor.

C. Raman spectra of disordered carbon samples

Raman measurements were performed with a micro-Raman setup in backscattering geometry. The laser light was focused in an inverted confocal microscope (Olympus IX71) by a 100× 1.4 N.A. Olympus objective into a diffraction limited spot on the sample. The 514 nm line of an Argon-ion laser (CVI Melles Griot 35MAP431-200) was used (0.25 mW on top of the objective). Spectra were collected with a Princeton Instruments SPEC 10:100 B/LN-eXcelon CCD detector and an SP 2356 spectrometer with 600 g/mm grating. An LL01-514 and FF01-520/5 filter (Semrock) was used to clean the laser light, a 30:70 beam splitter (XF122 Omega Optical) was used as dichroic mirror and 2 LP02-514RE filters (Semrock) were used to block the remaining laser light in the detection path. X-axis calibration was performed with a neon spectral lamp (6032 Newport). No *Y*-axis corrections or background removal procedures were performed. Only a constant value was added or subtracted for display purposes. The graphite reference sample was from Graphene Supermarket (Natural Kish Graphite Grade 300).

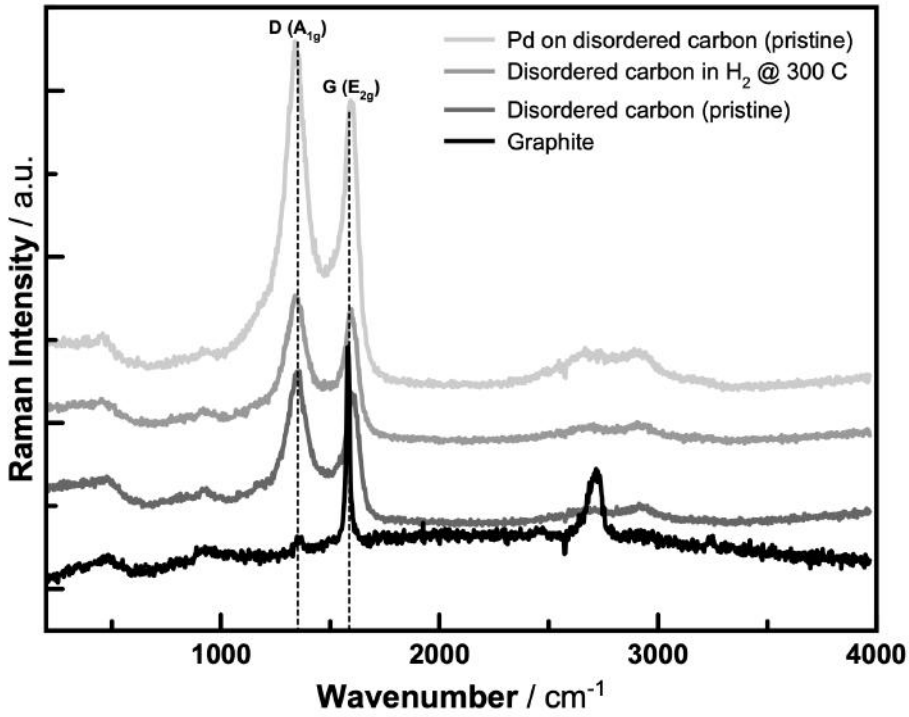

Fig. S5. Raman spectrum of disordered carbon samples exposed to different treatments. A graphite spectrum is measured for reference.

Raman spectroscopy has been used in the literature to monitor the graphitization process by following the peak ratio changes between the D and G modes at 1355 and 1581 cm^{-1}, respectively.[1] Roughly speaking, the G mode can be related to the presence of sp^2 in a perfect graphite structure, while the appearance of a D mode peak represents defective sp^2 hybridized carbon. Fig. S3 shows the Raman spectra of different disordered carbon samples together with a graphite sample as reference. As clearly illustrated, no significant changes in the I_D/I_G ratio are induced, when the samples are exposed to the different conditions used in the manuscript. The exposure to either a reducing atmosphere at elevated temperatures or the presence of metallic Pd is observed not to alter of disordered carbon support in any significant way as both the D and G modes ratios remain constant. Based on this, we can rule out the occurrence of any significant graphitization or increase in disorder.

D. PDF refinements of carbon-supported monometallic nanocrystals

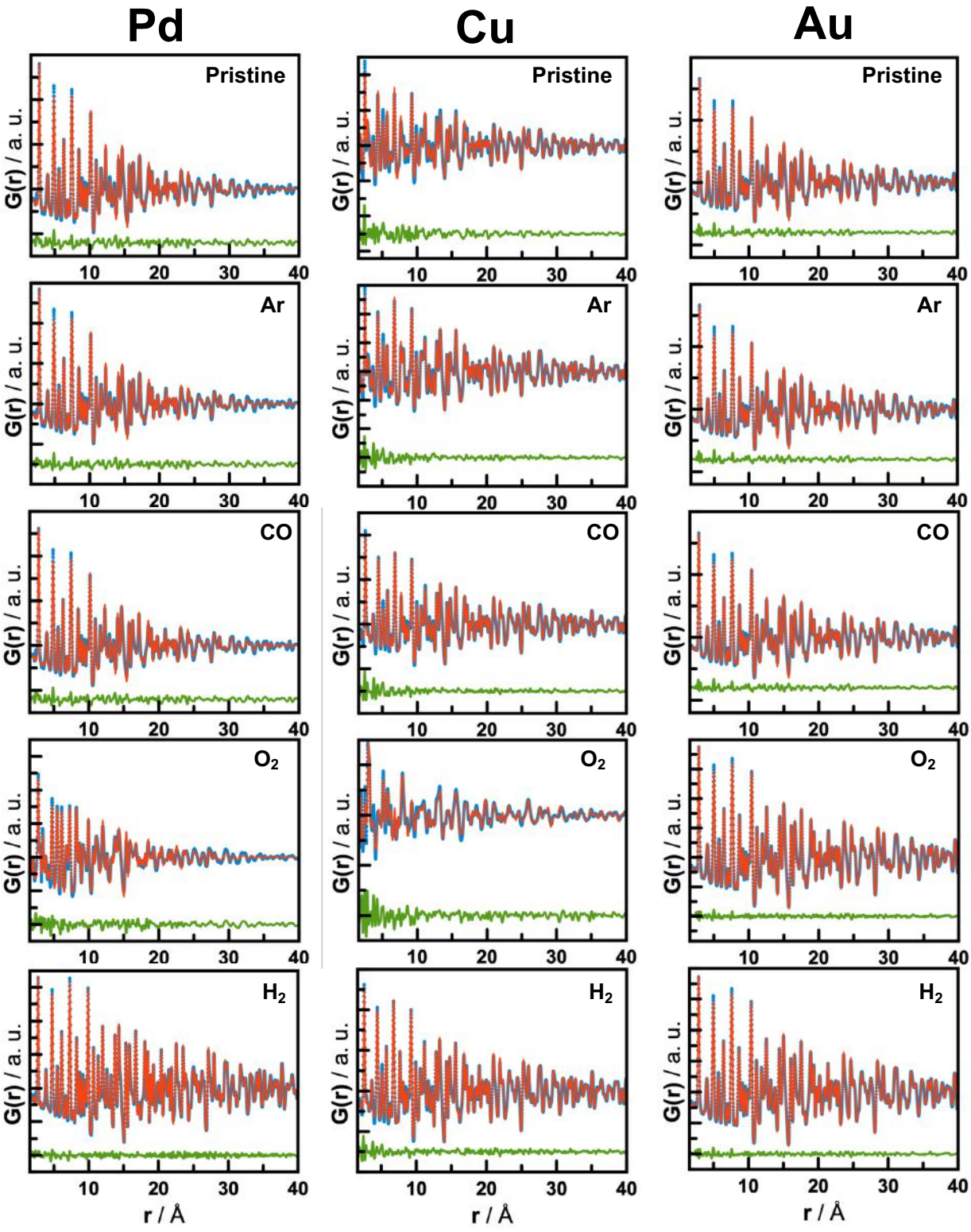

Fig. S6. PDF refinements of carbon-supported monometallic nanocrystals resulting from different gas exposures at 300 °C.

Table S7. Refined values from PDF refinements of carbon-supported Pd nanocrystals resulting from different gas exposures at 300 °C.

	Pristine	**Ar**	**CO**	**O_2**	**H_2**
R_{wp} / %	13.43	12.98	13.33	18.85	7.12
$Scale_{Pd}$	0.19	0.19	0.17	0.09	1.34×10^{-3} ($\pm0.13\times10^{-4}$)
δ_2	4.18	4.17	4.18	3.78	3.39
a_{Pd} / Å	3.99	3.99	3.99	3.89	3.89
U_{Pd} / Å^2	8.15×10^{-3}	8.18×10^{-3}	8.25×10^{-3}	8.89×10^{-3}	$5.94\cdot10^{-3}$
Crystallite $size_{Pd}$ / nm	5.07	5.08	5.19	4.44	21.50
$Scale_{PdO}$	-	-	-	0.06	-
a_{PdO} / Å	-	-	-	3.04	-
c_{PdO} / Å	-	-	-	5.36	-
U_{Pd} / Å^2	-	-	-	$7.97\cdot10^{-3}$	-
U_O / Å^2	-	-	-	$6.24\cdot10^{-2}$	-
Crystallite $size_{PdO}$ / nm	-	-	-	3.97	-
Phase composition (Pd/PdO) / %	-	-	-	47.02 / 52.98	-

Table S8. Refined values from PDF refinements of carbon-supported Cu nanocrystals resulting from different gas exposures at 300 °C.

	Pristine	**Ar**	**CO**	**O_2**	**H_2**
R_{wp} / %	22.83	16.31	14.69	36.44	10.37
$Scale_{Cu}$	0.14	0.17	0.23	0.05	0.30
δ_2	3.34	3.41	3.34	2.73	3.22
a_{Cu}/ Å	3.62	3.62	3.62	3.61	3.62
U_{Cu} / Å^2	9.19×10^{-3}	8.07×10^{-3}	8.07×10^{-3}	9.76×10^{-3}	7.62×10^{-3}
Crystallite $size_{Cu}$ / *nm*	9.05	10.56	10.27	5.08	13.45
$Scale_{CuO\ nano}$	0.12	-	-	0.12	-
$a_{CuO\ nano}$ / Å	4.88	-	-	4.74	-
$b_{CuO\ nano}$ / Å	2.99	-	-	3.50	-
$c_{CuO\ nano}$ / Å	4.98	-	-	5.11	-
$U_{Cu\ nano}$ / Å^2	6.85×10^{-3}	-	-	6.69×10^{-3}	-
$U_{O\ nano}$ / Å^2	9.49×10^{-4}	-	-	6.68×10^{-3}	-
$Y_{O1\ nano}$	0.59	-	-	0.71	-
$Y_{O2\ nano}$	0.41	-	-	0.29	-
$Y_{O3\ nano}$	0.09	-	-	0.21	-
$Y_{O4\ nano}$	0.91	-	-	0.79	-
Crystallite $size_{CuO\ nano}$ / nm	1.51	-	-	1.89	-
$Scale_{CuO\ bulk}$	0.07	-	-	0.06	-
$a_{CuO\ bulk}$ / Å	5.12	-	-	4.66	-
$b_{CuO\ bulk}$ / Å	3.73	-	-	3.45	-
$c_{CuO\ bulk}$ / Å	5.08	-	-	5.13	-
$U_{Cu\ bulk}$ / Å^2	1.57×10^{-2}	-	-	1.03×10^{-2}	-
$U_{O\ bulk}$ / Å^2	1.25×10^{-2}	-	-	2.46×10^{-3}	-
$Y_{O1\ bulk}$	0.58	-	-	0.55	-
$Y_{O2\ bulk}$	0.42	-	-	0.45	-
$Y_{O3\ bulk}$	0.08	-	-	0.05	-
$Y_{O4\ bulk}$	0.92	-	-	0.95	-
Crystallite $size_{CuO\ bulk}$ / nm	3.67	-	-	23.04	-
$Scale_{Cu2O}$	-	0.13	0.04	0.07	0.07
a_{Cu2O} / Å	-	4.27	4.24	4.26	4.24
U_{Cu} / Å^2	-	2.45×10^{-2}	2.55×10^{-2}	2.78×10^{-2}	2.71×10^{-2}
U_O / Å^2	-	2.62×10^{-1}	3.12×10^{-1}	$1.07\cdot10^{-1}$	5.42×10^{-1}
Crystallite $size_{Cu2O}$ / nm	-	6.11	3.82	10.63	2.29
Phase composition ($Cu/CuO_{nano}/CuO_{bulk}$) / %	33.02 / 42.42 / 24.56	-	-	-	-
Phase composition (Cu/Cu_2O) / %	-	49.25 / 50.75	82.11 / 17.89	-	77.49 / 22.51
Phase composition ($Cu/CuO_{nano}/CuO_{bulk}/Cu_2O$) / %	-	-	-	10.71 / 43.62 / 23.36 / 22.31	-

Table S9. Refined values from PDF refinements of carbon-supported Au nanocrystals resulting from different gas exposures at 300 °C.

	Pristine	**Ar**	**CO**	**O_2**	**H_2**
R_{wp} / %	10.32	10.05	9.96	6.18	5.96
δ_2	4.62	4.57	4.53	4.05	4.03
$Scale_{Au}$	5.89×10^{-1}	5.87×10^{-1}	5.85×10^{-1}	5.32×10^{-1}	5.24×10^{-1}
a_{Au} / Å	4.08	4.08	4.08	4.08	4.08
U_{Au} / Å^2	1.05×10^{-2}	1.03×10^{-2}	1.02×10^{-2}	9.16×10^{-3}	9.07×10^{-3}
Crystallite size / nm	8.16	8.99	9.36	17.15	18.58

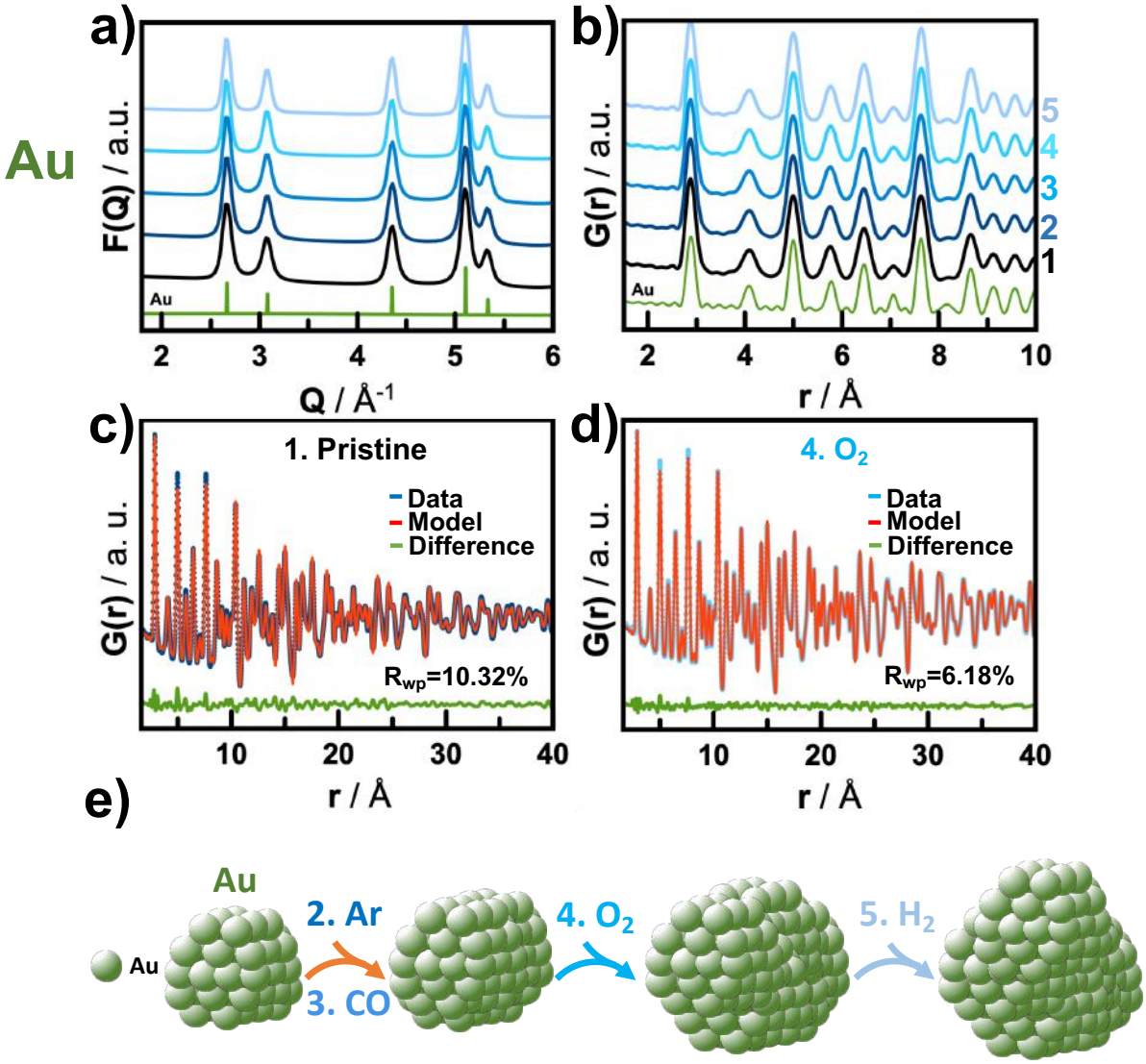

Fig. S7. *Ex situ* X-ray TS data of monometallic Au NCs supported on disordered carbon, which were annealed in varying atmospheres. The structural changes induced by the gas environments: 1 (pristine state, no gas), 2 (Ar), 3 (Ar-CO), 4 (Ar-CO-O_2) and 5 (Ar-CO-O_2-H_2) are shown in both (a) reciprocal space, $F(Q)$, and (b) real space, $G(r)$, together with PDF refinements of (c) pristine and (d) O_2-annealed NCs. (e) Schematic representation of the observed phase transformations.

E. PDF refinements of carbon-supported bimetallic nanocrystals

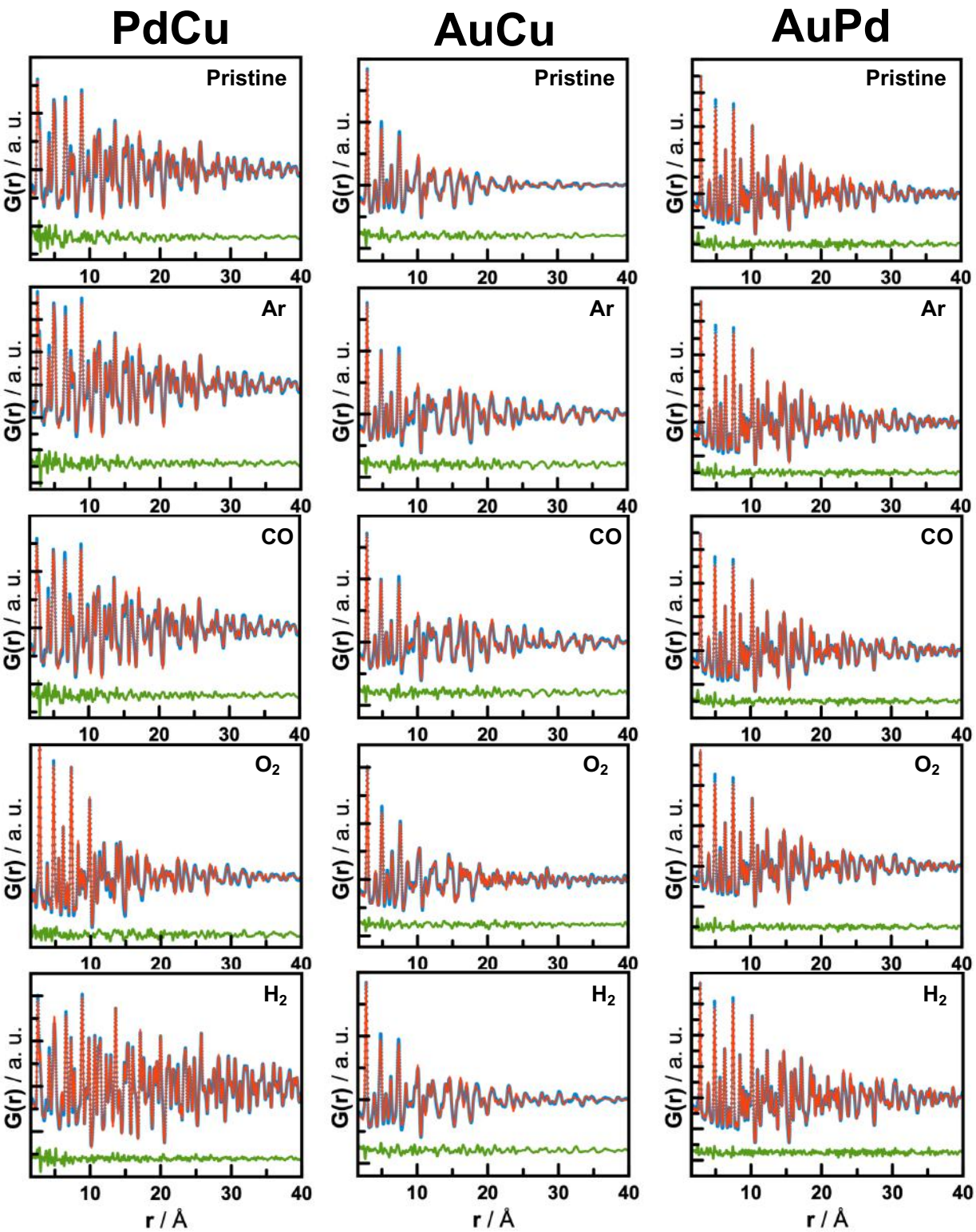

Fig. S8. PDF refinements of carbon-supported bimetallic nanocrystals resulting from different gas exposures at 300 °C.

Table S10. Refined values from PDF refinements of carbon-supported PdCu nanocrystals resulting from different gas exposures at 300 °C.

	Pristine	**Ar**	**CO**	**O_2**	**H_2**
R_{wp} / %	15.45	14.88	14.69	12.35	9.27
δ_2	3.94	3.98	3.99	2.55	3.41
$Scale_{B2}$	1.53×10^{-1}	1.46×10^{-1}	1.62×10^{-1}	2.59×10^{-2}	1.55×10^{-1}
a_{B2} / Å	2.98	2.98	2.98	2.98	2.98
U_{Pd} / Å^2	1.15×10^{-2}	1.18×10^{-2}	1.16×10^{-2}	7.29×10^{-3}	7.46×10^{-3}
U_{Cu} / Å^2	1.70×10^{-2}	1.74×10^{-2}	1.72×10^{-2}	3.14×10^{-2}	1.16×10^{-2}
Crystallite $size_{B2}$ / nm	7.01	6.83	6.99	3.32	25.01
$Scale_{Pd\ bulk}$	1.21×10^{-1}	7.23×10^{-2}	7.58×10^{-2}	1.21×10^{-1}	7.73×10^{-2}
$a_{Pd\ bulk}$ / Å	3.87	3.91	3.91	3.87	3.85
$U_{Pd\ bulk}$ / Å^2	2.36×10^{-2}	2.51×10^{-2}	2.42×10^{-2}	3.66×10^{-3}	1.24×10^{-2}
Crystallite $size_{Pd\ bulk}$ / nm	0.89	1.83	1.88	5.69	4.32
$Scale_{Pd\ nano}$	-	-	-	6.18×10^{-2}	-
$a_{Pd\ nano}$ / Å	-	-	-	3.87	-
$U_{Pd\ nano}$ / Å^2	-	-	-	3.66×10^{-3}	-
Crystallite $size_{Pd\ nano}$ / nm	-	-	-	1.51	-
$Scale_{CuO}$	-	-	-	4.20×10^{-2}	-
a_{CuO} / Å	-	-	-	4.66	-
b_{CuO} / Å	-	-	-	3.32	-
c_{CuO} / Å	-	-	-	6.46	-
U_{Cu} / Å^2	-	-	-	8.53×10^{-3}	-
U_O / Å^2	-	-	-	4.06×10^{-2}	-
Y_{O1}	-	-	-	0.41	-
Y_{O2}	-	-	-	0.59	-
Y_{O3}	-	-	-	-0.09	-
Y_{O4}	-	-	-	0.09	-
Crystallite $size_{CuO}$ / nm	-	-	-	1.37	-
Phase composition (B2/Pd) / %	60.24 / 39.76	70.79 / 29.21	71.92 / 28.08	-	70.72 / 29.28
Phase composition ($B2/Pd_{bulk}/Pd_{nano}/CuO$) / %	-	-	-	9.98 / 38.96 / 19.86 / 31.20	-

Table S11. Refined values from PDF refinements of carbon-supported AuCu nanocrystals resulting from different gas exposures at 300 °C.

	Pristine	**Ar**	**CO**	**O_2**	**H_2**
R_{wp} / %	14.59	16.56	16.41	12.36	14.89
δ_2	5.02	4.46	4.41	4.36	4.97
$Scale_{L10}$	3.61×10^{-1}	$5.23\cdot10^{-1}$	5.24×10^{-1}	-	4.28×10^{-1}
a_{L10} / Å	3.96	3.98	3.98	-	3.98
c_{L10} / Å	3.74	3.73	3.73	-	3.72
U_{Au} / Å^2	1.76×10^{-2}	1.65×10^{-2}	1.62×10^{-2}	-	2.02×10^{-2}
U_{Cu} / Å^2	3.07×10^{-2}	2.42×10^{-2}	2.38×10^{-2}	-	3.56×10^{-2}
Crystallite $size_{L10}$ / nm	5.59	10.70	10.90	-	6.45
$Scale_{Au}$	5.32×10^{-1}	2.93×10^{-1}	2.75×10^{-1}	3.61×10^{-1}	4.69×10^{-1}
a_{Au} / Å	3.99	3.95	3.95	4.08	3.97
U_{Au} / Å^2	1.69×10^{-2}	1.04×10^{-2}	1.01×10^{-2}	1.02×10^{-2}	1.53×10^{-2}
Crystallite $size_{Au}$ / nm	3.75	3.37	3.33	6.85	4.24
$Scale_{Au3Cu}$	-	-	-	4.98×10^{-1}	-
a_{Au3Cu} / Å	-	-	-	3.97	-
U_{Au} / Å^2	-	-	-	1.99×10^{-2}	-
U_{Cu} / Å^2	-	-	-	3.79×10^{-3}	-
Crystallite $size_{Au3Cu}$ / nm	-	-	-	5.49	-
$Scale_{CuO}$	-	-	-	1.02×10^{-2}	-
a_{CuO} / Å	-	-	-	4.37	-
b_{CuO} / Å	-	-	-	3.37	-
c_{CuO} / Å	-	-	-	5.09	-
U_{Cu} / Å^2	-	-	-	1.09×10^{-2}	-
U_O / Å^2	-	-	-	6.19×10^{-2}	-
Y_{O1}	-	-	-	0.03	-
Y_{O2}	-	-	-	0.97	-
Y_{O3}	-	-	-	-0.47	-
Y_{O4}	-	-	-	0.47	-
Crystallite $size_{CuO}$ / nm				2.29	
Phase composition ($L1_0$/Au) / %	48.98 / 51.02	71.64 / 28.36	72.95 / 27.05	-	56.41 / 43.59
Phase composition (Au_3Cu /Au/CuO) / %	-	-	-	58.49 / 36.13 / 5.38	-

Table S12. Refined values from PDF refinements of carbon-supported AuPd nanocrystals resulting from different gas exposures at 300 °C.

	Pristine	**Ar**	**CO**	**O_2**	**H_2**
R_{wp} / %	12.32	10.28	10.63	10.25	9.94
δ_2	4.13	4.25	4.26	4.40	3.81
$Scale_{AuPd}$	4.07×10^{-1}	3.72×10^{-1}	3.58×10^{-1}	2.89×10^{-1}	4.27×10^{-1}
a_{AuPd} / Å	3.99	3.99	3.99	3.99	3.99
U_{Au} / Å^2	6.06×10^{-3}	6.31×10^{-3}	6.31×10^{-3}	6.51×10^{-3}	5.85×10^{-3}
U_{Pd} / Å^2	1.43×10^{-2}	1.25×10^{-2}	1.24×10^{-2}	1.34×10^{-2}	1.18×10^{-2}
Crystallite $size_{AuPd}$ / nm	6.28	7.25	7.31	7.21	9.39
$Scale_{Au}$	6.96×10^{-2}	1.12×10^{-1}	1.05×10^{-1}	9.72×10^{-2}	5.30×10^{-2}
a_{Au} / Å	4.06	4.05	4.05	4.05	4.04
U_{Au} / Å^2	6.56×10^{-3}	9.25×10^{-3}	9.08×10^{-3}	9.21×10^{-3}	5.47×10^{-3}
Crystallite $size_{Au}$ / nm	5.45	5.83	5.89	5.86	7.89
Phase composition (AuPd/Au) / %	87.79 / 12.21	80.37 / 19.63	80.77 / 19.23	78.55 /21.45	90.83 / 9.17

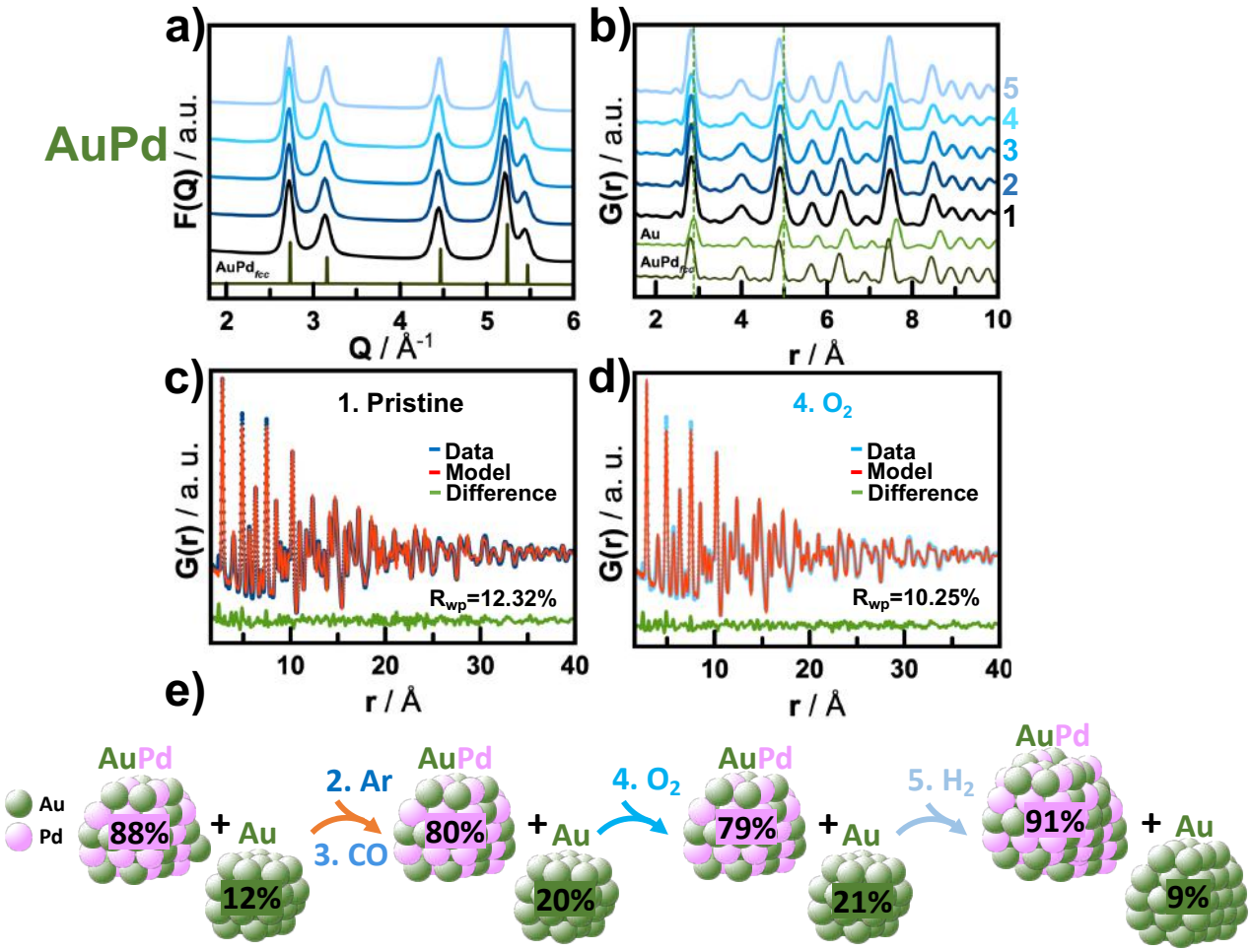

Fig. S9. *Ex situ* X-ray TS data of monometallic AuPd NCs supported on disordered carbon, which were annealed in varying atmospheres. The structural changes induced by the gas environments: 1 (pristine state, no gas), 2 (Ar), 3 (Ar-CO), 4 (Ar-CO-O_2) and 5 (Ar-CO-O_2-H_2) are shown in both (a) reciprocal space, $F(Q)$, and (b) real space, $G(r)$, together with PDF refinements of (c) pristine and (d) O_2-annealed NCs. (e) Schematic representation of the observed phase transformations.

F. ICP-OES measurements

Table S13. Amount of metals present in the carbon-supported bimetallic nanocrystals from ICP-OES analysis.

	Au / ppm	**Pd** / ppm	**Cu** / ppm	**Au loading** / wt.%	**Pd loading** / wt.%	**Cu loading** / wt.%	**% Au in alloy** / %	**% Pd in alloy** / %	**% Cu in alloy** / %
PdCu	-	120.63	39.42	-	0.01	$0.04 \cdot 10^{-1}$	-	16.31	83.69
AuCu	274.14	-	53.44	0.03	-	$0.05 \cdot 10^{-1}$	75.37	-	24.63
AuPd	0.14	52.51	-	$1.36 \cdot 10^{-5}$	$0.05 \cdot 10^{-1}$	-	0.27	99.73	-

Inductively coupled plasma-optical emission spectrometry (ICP-OES) was conducted using a Thermofisher scientific iCAP Pro series instrument to determine the actual metal content and ratio. Prior to analysis, the bimetallic NC samples were dissolved in 4 mL aqua regia, and digested for 4 hours. Afterwards, 2 mL of Suprapur nitric acid (65%, Sigma-Aldrich) was added, followed by evaporation until the samples were almost dry. Thereafter, 1 mL of hydrogen peroxide was added, and evaporated, followed by addition of MilliQ water. The samples were centrifugated, filtered to remove undissolved carbon and diluted with MilliQ water.

For AuPd, we here note the discrepancy between the low Au content in the ICP-OES measurements, and the identification of monometallic Au in the experimental PDFs. A reason for the lower Au content might be related to the difficulty of fully dissolving the sample, where a loss of Au might have occurred upon filtering away residual carbon, which was not dissolved.

G. Identifying nanocrystal structures with high-resolution transmission electron microscopy

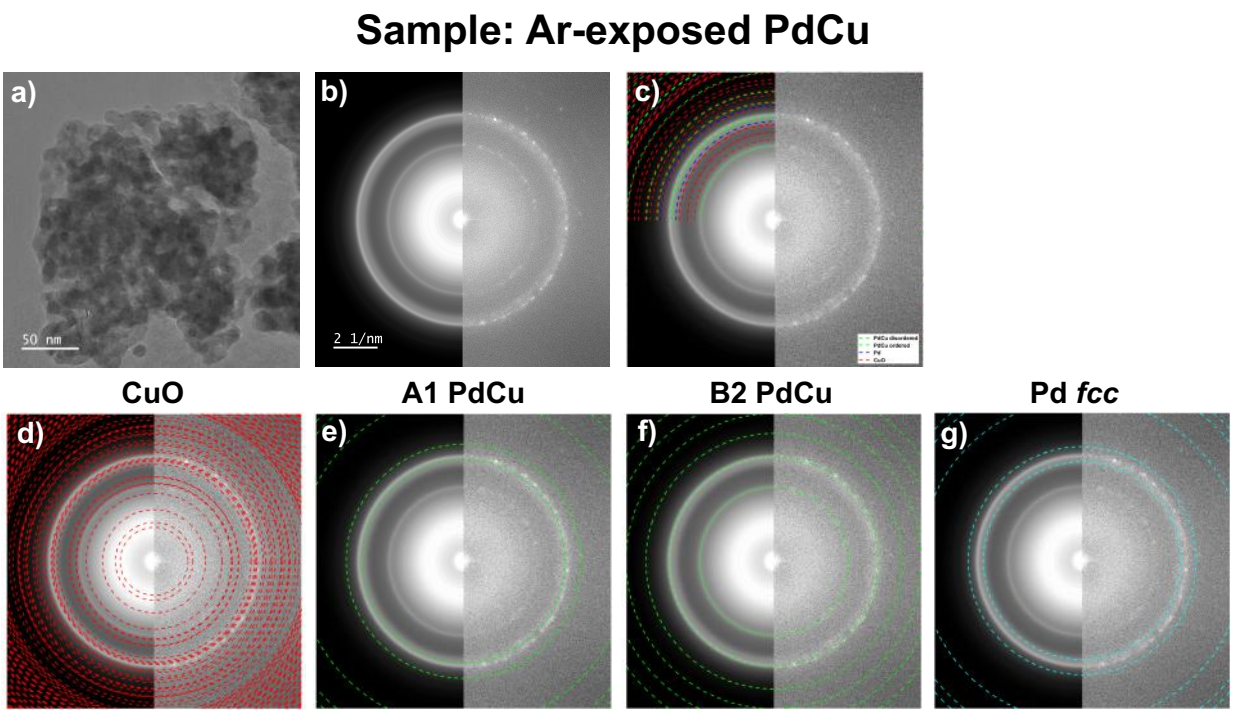

Fig. S10. HR-TEM image and Fast Fourier transform (FFT) (left) with and (right) without radially averaged intensity profiles of PdCu NC agglomerates exposed to Ar. (a) shows the HR-TEM image of PdCu NCs, while (b) presents the FFT of the NCs, and (c) shows the FFT with the crystal structure lattice spacings of previously identified phases overlaid. (d-g) shows the FFT with the lattice spacings of the individual crystal structures overlaid.

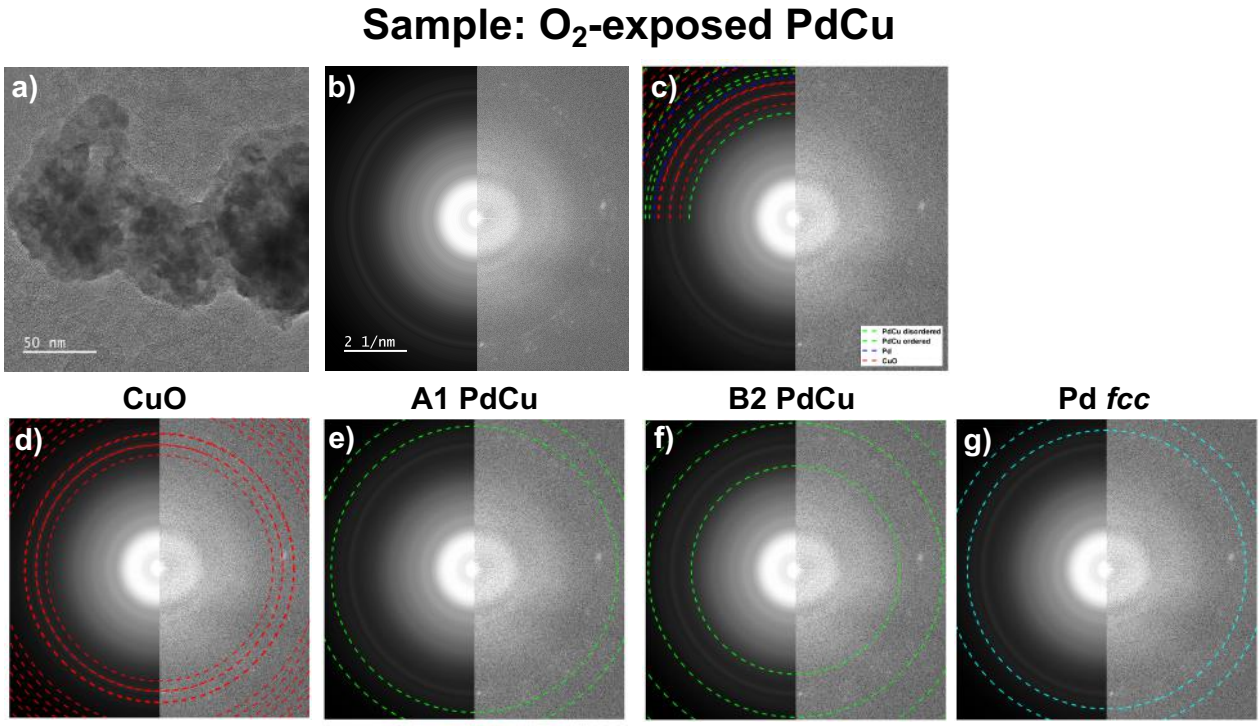

Fig. S11. HR-TEM image and FFT (left) with and (right) without radially averaged intensity profiles of PdCu NC agglomerates exposed to O_2. (a) shows the HR-TEM image of PdCu NCs, while (b) presents the FFT of the NCs, and (c) shows the FFT with the crystal structure lattice spacings of previously identified phases overlaid. (d-g) shows the FFT with the lattice spacings of the individual crystal structures overlaid.

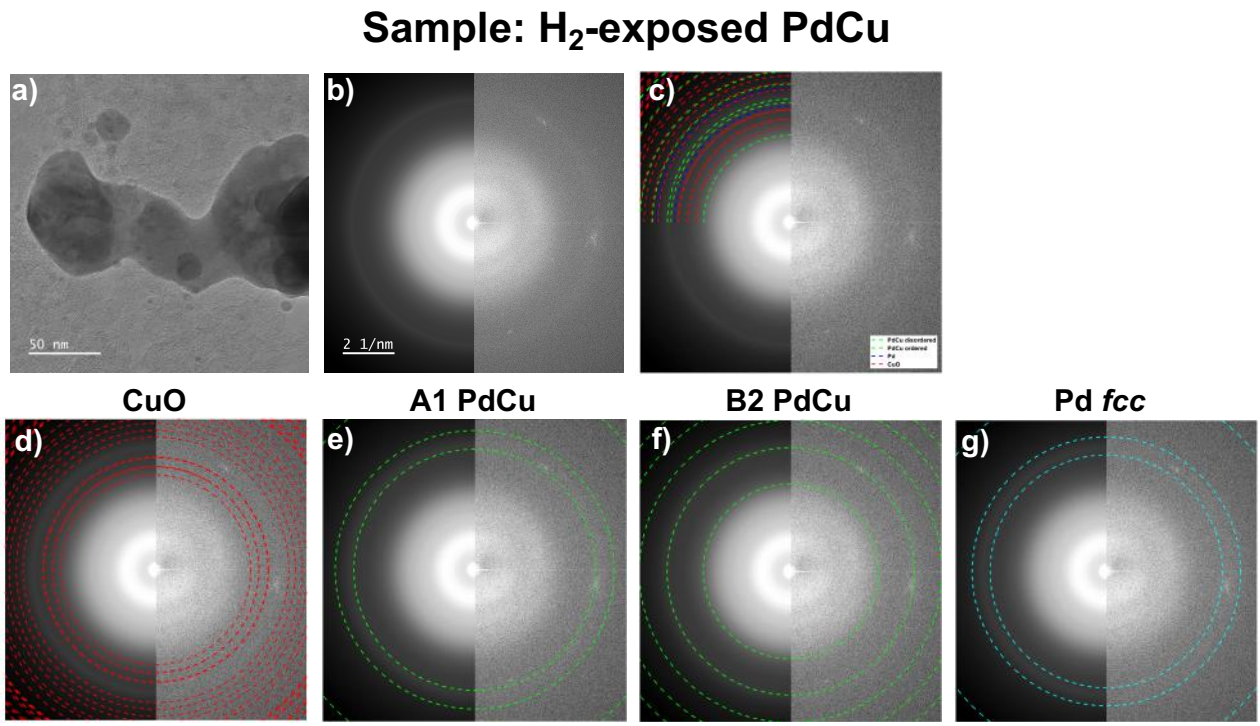

Fig. S12. HR-TEM image and FFT (left) with and (right) without radially averaged intensity profiles of PdCu NC agglomerates exposed to H_2. (a) shows the HR-TEM image of PdCu NCs, while (b) presents the FFT of the NCs, and (c) shows the FFT with the crystal structure lattice spacings of previously identified phases overlaid. (d-g) shows the FFT with the lattice spacings of the individual crystal structures overlaid.

Table S14. Comparison of relevant lattice spacings for selected *hkl*-reflections of identified phases for gas-exposed AuCu and PdCu NCs.

(*hkl*)	[2] B2 PdCu / Å	[3] Pd / Å	[4] CuO / Å	[5] $L1_0$ AuCu / Å	[6] Au_3Cu / Å	[7] Au / Å
(100)	2.99	1.94*	2.53*	3.67	3.98	2.04*
(110)	2.11	1.37**	2.75	2.80	2.81	1.44**
(111)	1.73	2.24	2.32	2.23	2.29	2.36

*Listed for the (002) reflection.
**Listed for the (022) reflection.

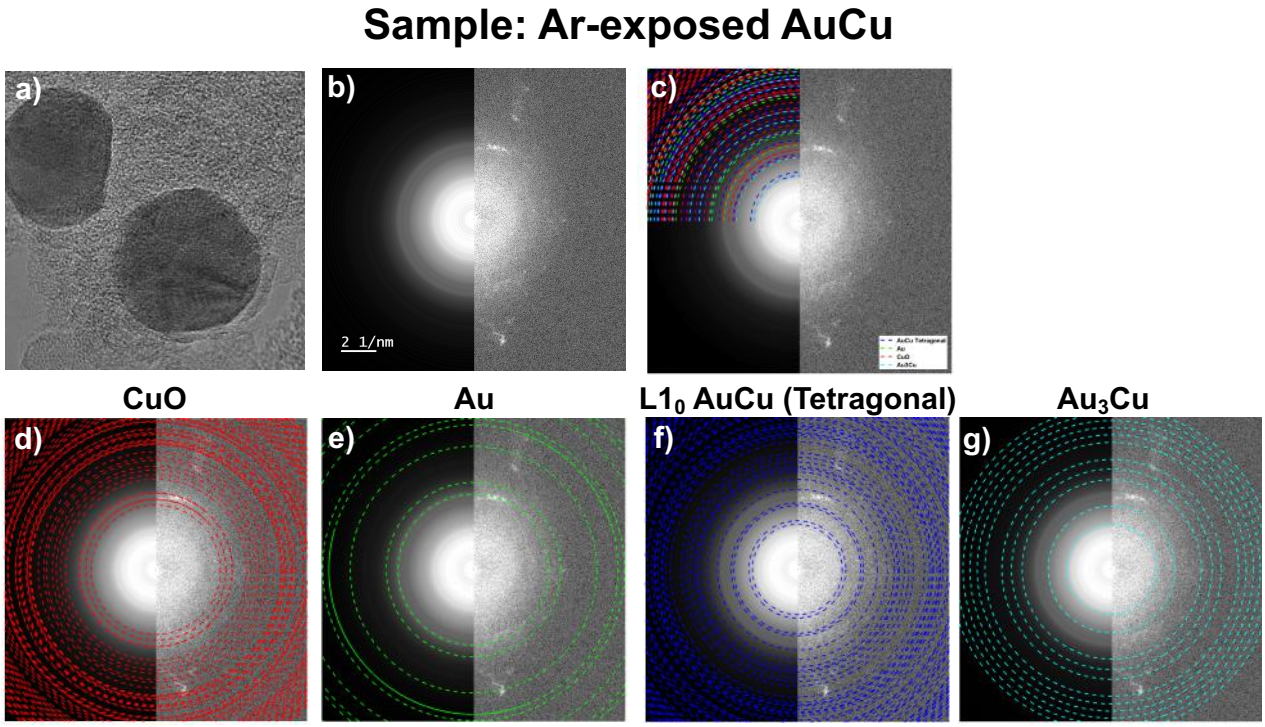

Fig. S13. HR-TEM image and FFT (left) with and (right) without radially averaged intensity profiles of AuCu NC agglomerates exposed to Ar. (a) shows the HR-TEM image of AuCu NCs, while (b) presents the FFT of the NCs, and (c) shows the FFT with the crystal structure lattice spacings of previously identified phases overlaid. (d-g) shows the FFT with the lattice spacings of the individual crystal structures overlaid.

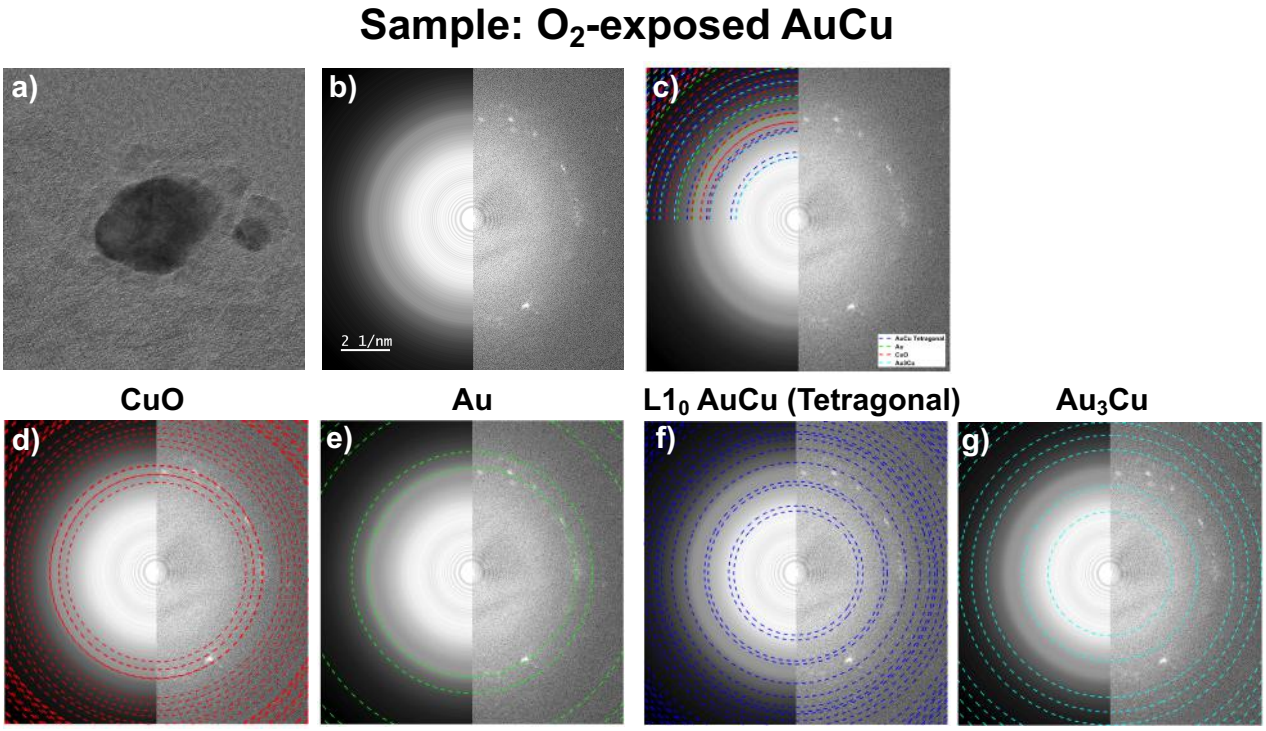

Fig. S14. HR-TEM image and FFT (left) with and (right) without radially averaged intensity profiles of AuCu NC agglomerates exposed to O_2. (a) shows the HR-TEM image of AuCu NCs, while (b) presents the FFT of the NCs, and (c) shows the FFT with the crystal structure lattice spacings of previously identified phases overlaid. (d-g) shows the FFT with the lattice spacings of the individual crystal structures overlaid.

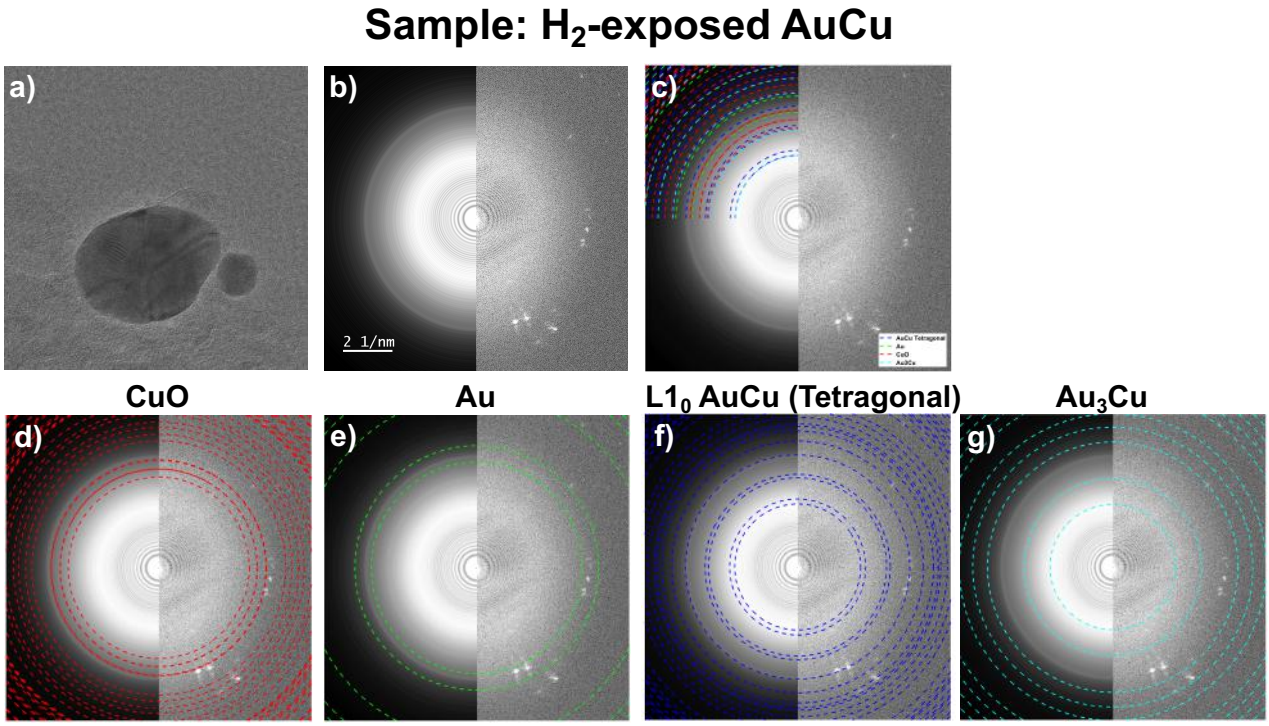

Fig. S15. HR-TEM image and FFT (left) with and (right) without radially averaged intensity profiles of AuCu NC agglomerates exposed to H_2. (a) shows the HR-TEM image of AuCu NCs, while (b) presents the FFT of the NCs, and (c) shows the FFT with the crystal structure lattice spacings of previously identified phases overlaid. (d-g) shows the FFT with the lattice spacings of the individual crystal structures overlaid.

H. Gibbs free energy calculations

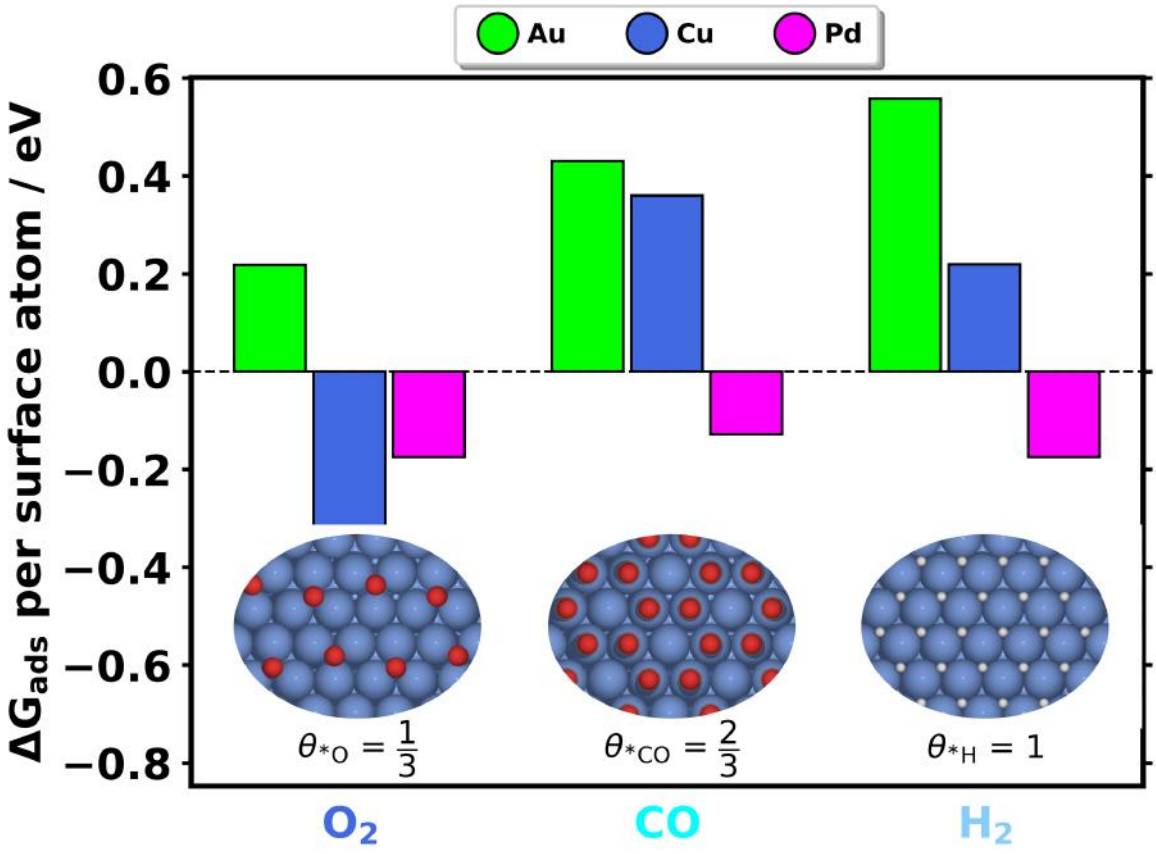

Fig. S16. Gibbs free energy of Au (green), Cu (blue) and Pd (magenta) in O_2, CO and H_2 gas environments.

The calculations present the stability of the metals in the varying gas environments. For a metal to be stable, the Gibbs free energy needs to be negative. Therefore, **Fig. S14** shows that in an O_2 atmosphere, Cu is most stable, while in CO and H_2 Pd will show the highest degree of stability.

I. HH-TEM data analysis procedure for AuCu

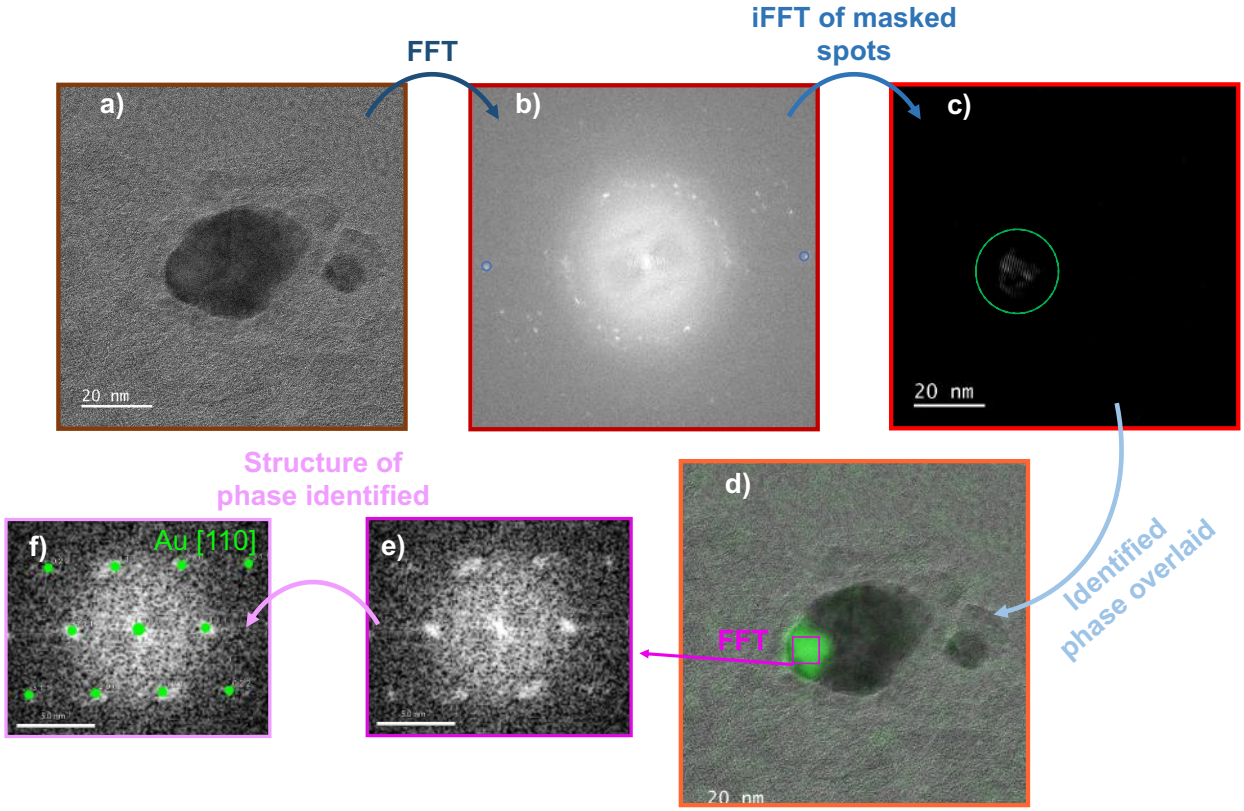

Fig. S17. The HR-TEM data analysis procedure for AuCu, when lattice spacings overlap in the FFTs. (a) From the HR-TEM image, an (b) Fast Fourier transform (FFT) image was made. Each spot was chosen and masked in the FFT (blue rings in (b)). (c) An inverse FFT (iFFT) of the selected spots was made, and resulting image was overlaid with the HR-TEM image to localize the spatial origin of the spots (d). (e) shows the FFT of the selected region of interest, which is analysed to find the phase and zone-axis (f). We note here the presence of halos in the central part of the FFT in (b). These correspond to the structure or object folded by the contrast transfer function of the microscope, which provides a background contribution that stems from the information transfer through the microscope.

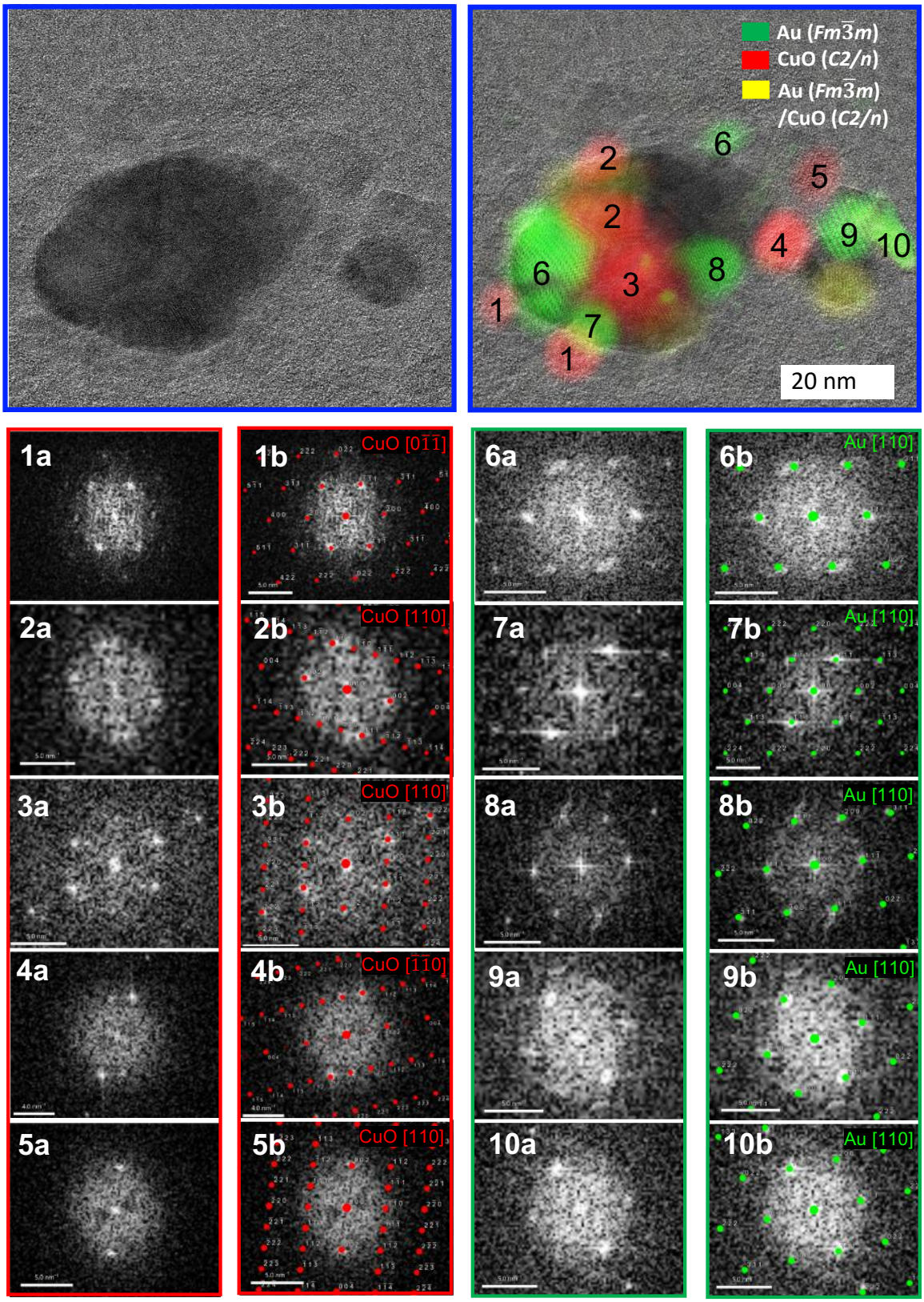

Fig. S18. (Top) HR-TEM image before and after overlaid iFFTs. (Bottom, 1-10) (a) The FFTs of the selected regions of interest with (b) phases and zone-axes as indicated

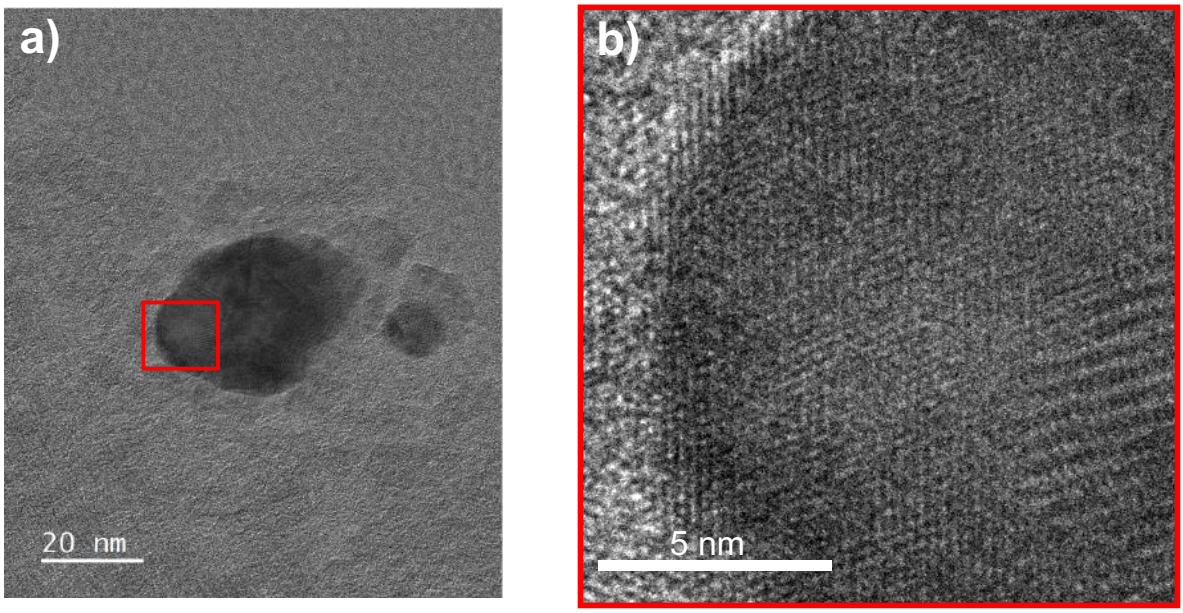

Fig. S19. (a) HR-TEM image of AuCu NC agglomerates exposed to O_2. (b) shows a digital zoomed image of the highlighted region in (a), which clearly illustrates the presence of HR information from the lattice fringes in the NC.

References:

1. A. C. Ferrari and J. Robertson, *Phys. Rev. B*, 2000, **61**, 14095.
2. M. Yamauchi and T. Tsukuda, *Dalton Transactions*, 2011, **40**, 4842-4845.
3. G. Bredig and R. Allolio, *Z. Phys. Chem.*, 1927, **126**, 41-71.
4. S. Åsbrink and L.-J. Norrby, *Acta Crystallographica Section B: Structural Crystallography and Crystal Chemistry*, 1970, **26**, 8-15.
5. I. Uszyński, J. Janczak and R. Kubiak, *J. Alloys Compd.*, 1994, **206**, 211-213.
6. R. Kubiak and J. Janczak, *J. Alloys Compd.*, 1991, **176**, 133-140.
7. E. Owen and E. Yates, *The London, Edinburgh, and Dublin Philosophical Magazine and Journal of Science*, 1933, **15**, 472-488.